

Article

Grain Growth upon Annealing and Its Influence on Biodegradation Rate for Pure Iron

Yu Zhang ^{1,2}, Ke Zhang ^{1,2}, Weidong Liu ^{1,3,*}, Zhongren Zheng ⁴ and Mingchun Zhao ⁴ ¹ Xiangya Hospital, Central South University, Changsha 410008, China² National Clinical Research Center for Geriatric Disorders, Xiangya Hospital, Changsha 410008, China³ International Joint Research Center of Minimally Invasive Endoscopic Technology Equipment & Standards, Changsha 410008, China⁴ School of Materials Science and Engineering, Central South University, Changsha 410083, China

* Correspondence: weidong.liu@csu.edu.cn

Abstract: Biodegradable pure iron has gained significant interest as a biomedical material. For biodegradable implant applications, the biodegradation behavior of pure iron is important. In this work, the influence of ferrite grain size on the biodegradation rate for pure iron was studied by means of heat treatment that was annealed below the austenized temperature using as-forged pure iron. Grains were coarsened and a spectrum of ferrite grain sizes was gained by changing the annealed temperature. Biodegradation behavior was studied through weight loss tests, electrochemical measurements and microscopic analyses. Hardness (HV) and biodegradation rate (P_i or P_w) were linearly ferrite grain size-dependent: $HV = 58.9 + 383.2d^{-\frac{1}{2}}$, and $P_i = -0.023 + 0.425d^{-\frac{1}{2}}$ or $P_w = 0.056 + 0.631d^{-\frac{1}{2}}$. The mechanism by which the role of grain size on biodegradation rate was attributed to the ferrite grain boundary traits.

Keywords: pure iron; annealing; grain refinement; biodegradation; implant material

Citation: Zhang, Y.; Zhang, K.; Liu, W.; Zheng, Z.; Zhao, M. Grain Growth upon Annealing and Its Influence on Biodegradation Rate for Pure Iron. *Materials* **2022**, *15*, 8030. <https://doi.org/10.3390/ma15228030>

Academic Editors: Francesco Baino and Yuri Sharkeev

Received: 21 August 2022

Accepted: 31 October 2022

Published: 14 November 2022

Publisher's Note: MDPI stays neutral with regard to jurisdictional claims in published maps and institutional affiliations.



Copyright: © 2022 by the authors. Licensee MDPI, Basel, Switzerland. This article is an open access article distributed under the terms and conditions of the Creative Commons Attribution (CC BY) license (<https://creativecommons.org/licenses/by/4.0/>).

1. Introduction

Biodegradable pure iron has recently gained significant interest in terms of its use in medical devices, such as bone scaffolds, fixtures and stents due to its good mechanical properties and biocompatibility in physiological environments, which provides sufficient temporary support to resist the applied load and effectively eliminates the potential risk of long-term complications through the progressive degradation in the body [1–3]. The degradable and absorbable functions for pure iron are highly desired because they do not need a secondary surgical procedure for the removal, which easily increases risk of the infection, surgical cost, and the likelihood of patient complications.

Work concerning the biodegradable implant applications of pure iron has involved in the conventional manufacturing procedures, such as microwave sintering, laser melting, casting and deformation processing [4–7]. Manufacturing processes play a fundamental role towards the biodegradation of pure iron. Zhao et al. comparatively studied the biodegradation behavior of pure iron prepared by microwave sintering (MS) and laser melting (LM) and found that the biodegradation rate of the MSed Fe was higher than that of the LMed Fe and their biodegradation rates were higher than that of the as-cast Fe [4]. Carluccio et al. [5] reported that the biodegradation rate of the pure iron manufactured via selective laser melting was over 50% higher than the corresponding cast equivalent. Bagherifard et al. [6] found that the inclined and multi-directional surface impacts accelerated the biodegradation of pure iron. Obayi et al. [7] studied the influence of the cross-rolling on the biodegradation of pure iron as biodegradable material for medical implants and found that the biodegradation was more uniform for the cross-rolled samples while the biodegradation rates between the cross-rolled samples and the straight-rolled samples did not show relevant differences in simulated body solution. Such conventional manufacturing methods

often need further the post processing, such as annealing, to obtain the final product. It is known that the annealing of the metals has an important impact on the microstructural factors, such as grain size, sub-structures, internal stresses, macro-segregations, impure inclusions and second phase particles, each of which might have an impact on the mechanical properties and the degradation response. The annealing of pure iron only needs reheating to a temperature below the austenized temperature for several hours, followed by air cooling. The mechanical properties and biodegradation behavior of pure iron are important for biodegradable implant applications. It is well established that the mechanical properties of pure iron were significantly influenced by annealing [8]. However, only little work has reported on the biodegradation behavior of pure iron upon annealing [9], and the details of grain growth upon annealing and its influence on biodegradation rate for pure iron is not yet fully understood, which restrains pure iron as biodegradable implant materials to meet the requirements of clinical applications. The biodegradation rate dependence of the grain size of pure iron is worthy of study. However, most work to date has only studied coarse and/or fine grain size but not a spectrum of grain size.

In this work, pure iron was annealed at different annealing temperature to obtain a spectrum of ferrite grain size, and grain growth upon annealing and its influence on the biodegradation rate of pure iron was studied. The mechanism by which the role of the ferrite grain size on the biodegradation rate of pure iron was revealed. This work provides a reference to regulate the biodegradation behavior of pure iron through annealing and facilitates its use in biodegradable implant applications.

2. Experiments

Pure iron (provided by Institute of Metal Research, Chinese Academy of Science, Shenyang city, China) was used in this work at a high purity, with a chemical composition (wt.%) of 0.006 C, 0.002 Mn, 0.003 Si, 0.005 P, 0.005 S, 0.003 Ni, 0.002 Cr, 0.009 Ti, 0.002 Cu and Fe balance. Specimens of 10 mm diameter and 3 mm length were cut from the forged rods, which were hot-forged from the initial as-cast ingots. Annealing was performed for the forged specimens at 765, 785 and 805 °C for 2 h, followed by furnace cooling to 650 °C then air cooling, respectively. A schematic annealing procedure diagram is shown in Figure 1. Hereafter, three annealed conditions are designed as Fe765, Fe785 and Fe805, respectively. The microstructure was examined by optical microscopy by etching the mechanically polished surfaces of metallographic specimens using nitric acid alcohol with a 2% concentration. The microstructure was also characterized by electron back-scattered diffraction (EBSD). The hardness was tested using a digital Vickers indenter.

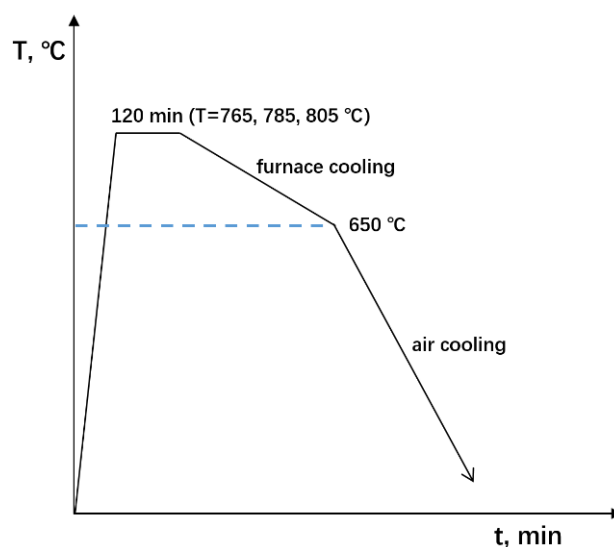


Figure 1. Schematic annealing procedure diagram.

Potentiodynamic polarization test was conducted in Hank's solution at 37 ± 0.5 °C through an Autolab system using a common three-electrode system with platinum as the counter electrode, saturated calomel as reference electrode (SCE) and the specimen as working electrode. The electrochemical impedance spectrum (EIS) was measured after open-circuit potential (OCP) had been stable for 3600 s. The biodegradation rate, P_i (mm y^{-1}), was calculated by Equation (1) using the corrosion current density measured, i_{corr} (mA cm^{-2}), from potentiodynamic polarization curves [10,11]:

$$P_i = 11.16i_{corr} \quad (1)$$

Immersion test was performed in Hank's solution for 14 days at 37 ± 0.5 °C. The weight loss rate, ΔW ($\text{mg cm}^{-2} \text{d}^{-1}$), was calculated by Equation (2), and the biodegradation rate, P_w (mm y^{-1}), was calculated by Equation (3), respectively [10,11].

$$\Delta W = (W_b - W_a) / AT \quad (2)$$

$$P_w = 3.67 \Delta W / D \quad (3)$$

where W_b and W_a are the specimen mass before exposure and after exposure, respectively; A is the specimen area exposed to the corrosive solution (cm^2); T is the time (d); and D is the density of the material in g/cm^3 (7.87 g/cm^3 for pure iron). Corroded surface morphology was observed using a scanning electron microscopy and corroded topographic map was characterized using a 3D-measuring laser microscope.

3. Results

3.1. Grain Growth and Hardness Variation

Figure 2 shows the optical micrographs of the initial forged condition (Figure 2a) and the different annealed conditions (Figure 2b–d). There were no apparent inclusions or second phase particles in the matrix for all the microstructures. This indicated that the experimental pure iron was very clean and the influence of impure inclusions on its biodegradation was expected to be negligible.

As shown in Figure 2a, the initial forged condition presented some sub-structures or sub-grains in microstructure. Figure 3a,b shows the EBSD-characterized ferrite grain boundaries and the IPF map of the initial forged condition. The black lines indicated mis-orientations over 15° between the adjacent points (i.e., high angle grain boundary), and the green lines reflected the mis-orientations between 1 and 15° (i.e., low angle grain boundary). High angle grain boundaries were accompanied by large numbers of low angle grain boundaries. Therefore, the forged pure iron essentially accumulated a large number of sub-structures or sub-grains during deformation. When the forged pure iron was annealed, the nuclei were generated at the subgrain or grain boundaries of the original deformed microstructure, and the new undistorted ferrite grains with little residual stress and low dislocation density were formed, i.e., the growth of ferrite grains [12]. All the annealed microstructures consisted of quasi-polygonal ferrite grains, as shown in Figure 2b–d. Figure 3c,d shows the EBSD-characterized ferrite grain boundaries and the IPF map of the representative annealed condition of Fe765. The low angle grain boundaries almost disappeared in microstructure.

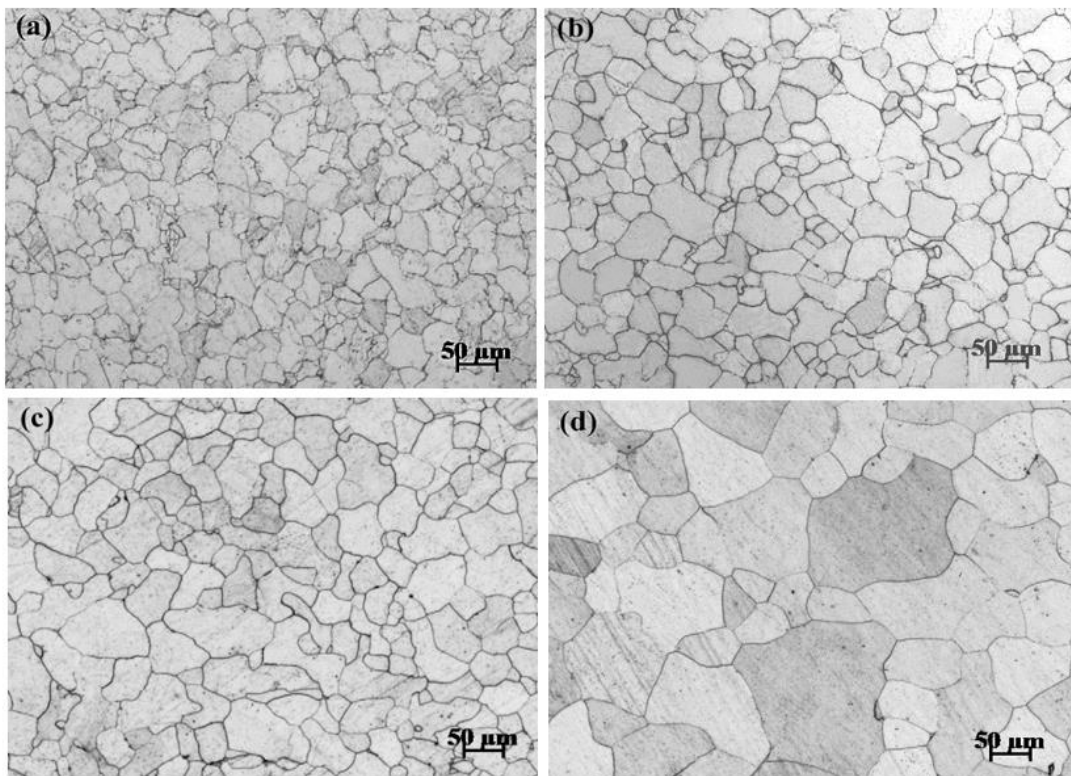


Figure 2. Optical micrographs at (a) the initial forged condition and (b–d) the different annealed conditions: (b) 765 °C, (c) 785 °C, (d) 805 °C.

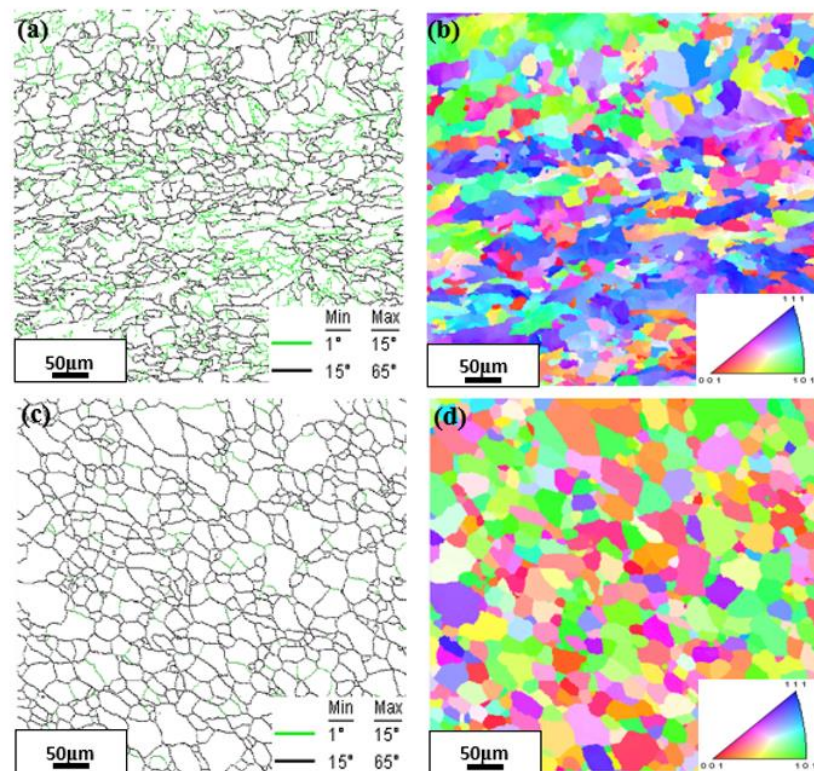


Figure 3. (a) the EBSD-characterized grain boundaries and (b) the IPF map of the initial forged condition; (c) the EBSD-characterized grain boundaries and (d) the IPF map of the representative annealed condition of Fe765.

Figure 4 shows the average ferrite grain size in the initial forged condition and subsequent annealed conditions. Average ferrite grain size in the initial forged condition was 27 μm . A pronounced evolution of the ferrite grain size was presented when the annealed temperature changed. The driving force of the regenerated undistorted ferrite grains became higher at a higher annealed temperature, forming the new undistorted larger grains. As annealed at 765 $^{\circ}\text{C}$, average ferrite grain size was 33 μm . The increasing annealed temperature caused the coarsening of the ferrite grain size. As annealed at 785 $^{\circ}\text{C}$ and 805 $^{\circ}\text{C}$, the average ferrite grain size was 43 μm and 82 μm , respectively. Figure 4 also depicts the Vickers hardness values of the forged and different annealed conditions. For the forged condition, the hardness was 134.6 HV. The hardness changed when the annealed temperature changed. As annealed at 765 $^{\circ}\text{C}$, the hardness was 123.9 HV. As annealed at 785 $^{\circ}\text{C}$ and 805 $^{\circ}\text{C}$, the hardness was 116.1 HV and 102.2 HV, respectively. The hardness decreased with the increase of the annealed temperature. The ferrite grain size increased with the increase of the annealed temperature, as mentioned above. Therefore, the hardness decreased with increasing the ferrite grain size. The grain boundaries blocked the dislocation movement. A smaller grain size presented a larger grain boundary proportion, with a more obvious hindrance [13]. The regression equation that described the relationship between ferrite grain size and hardness was obtained as Equation (4) had a correlation coefficient in 0.99, using all the measured data.

$$\text{HV} = 58.9 + 383.2d^{-\frac{1}{2}} \quad (4)$$

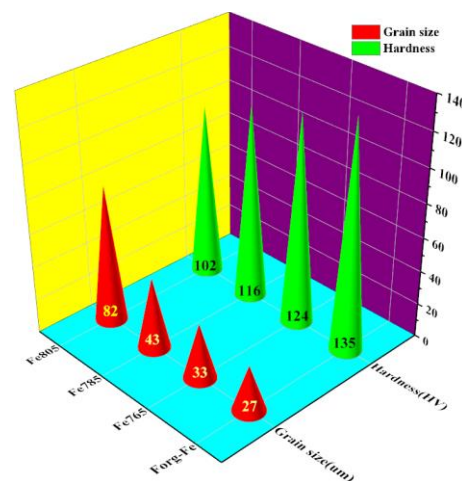


Figure 4. Average grain size and Vickers hardness at different annealed conditions (Fe765, Fe785, and Fe805), with the forged condition (Forg-Fe) as a comparison.

The hardness value of pure iron was linearly ferrite grain size-dependent, following a so-called Hall–Petch relation [14].

3.2. Biodegradation

Figure 5a depicts potentiodynamic polarization curves for the specimens at different annealed temperatures in Hank's solution. The corrosion potential (E_{corr}) value had little change for the specimens at different annealed temperature. The E_{corr} value can reflect the thermodynamic information of the corrosion and can thus reflect the biodegradable tendency. The E_{corr} value of the metal is related to such internal states as the residual stress, the deformed twins and texture, etc [15]. A similar E_{corr} value for the specimens at different annealed temperatures in the present work indicated that there had been a similar internal state, which means that the designed annealed conditions excluded the effects of other structure factors from the processing, such as sub-structures, internal stresses, residual stress, twins and texture. The i_{corr} values of the specimens at the different annealed

temperature had relatively obvious differences, which were measured from the linear cathodic branch of polarization potential curves according to Tafel extrapolation and are shown in Table 1. The i_{corr} value decreased with the increase of the annealed temperature.

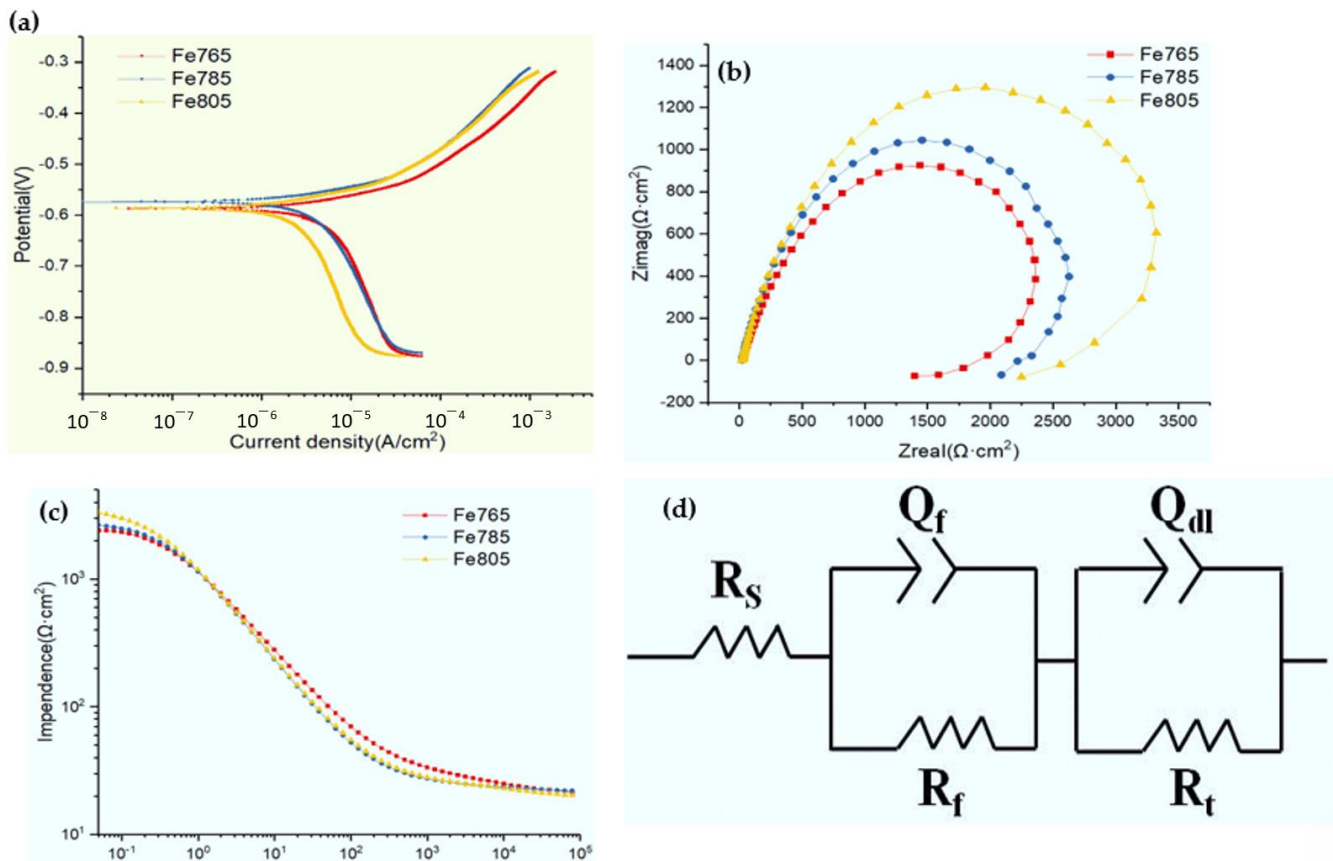


Figure 5. (a) Polarization curves, (b) Nyquist plots and (c) Bode plots of the different annealed conditions in Hank's solution and (d) the equivalent circuit for impedance data fitting.

Table 1. Polarization data of the different annealed conditions in Hank's solution.

Specimens No.	E_{corr} (V _{SCE})	i_{corr} (μ A/cm ²)
Fe765	−0.587	4.686
Fe785	−0.574	3.514
Fe805	−0.586	2.196

Figure 5b,c shows the electrochemical impedance spectra (EIS) data of the specimens at the different annealed temperature in Hank's solution. The shape of the Nyquist plots are similar for the specimens at the different annealed temperature, with one single capacitive loop in the measured frequency range. The corresponding capacitive loop diameter was involved in the anti-polarization. A larger capacitive loop diameter reflected a lower corrosion rate [16,17]. The diameter size order increased with the increase of the annealed temperature. The equivalent circuit that can be used to study the Nyquist spectra is illustrated in Figure 5d. The corresponding results are shown in Table 2, in which R_t is the charge transfer resistance, R_s is the solution resistance, CPE_{dl} is the double-layer capacitor, R_f is the film resistance and CPE_f is the capacitance that reflects the effect of the surface film. The R_t value order is Fe805 > Fe785 > Fe765, corresponding to the size order of the above-mentioned EIS spectra diameter.

Table 2. Parameters obtained from the simulation circuit in Hank's solution.

Specimen No.	R_S ($\Omega \text{ cm}^2$)	CPEfilm-T ($\Omega^{-1} \text{ s}^{-n}/\text{cm}^2$)	n	R_f ($\Omega \text{ cm}^2$)	CPEct-T ($\Omega^{-1} \text{ s}^{-n}/\text{cm}^2$)	n	R_t ($\Omega \text{ cm}^2$)
Fe765	20.47	6.339×10^{-5}	0.692	15.11	1.275×10^{-4}	0.724	2.822×10^3
Fe785	21.79	1.59×10^{-4}	0.708	14.38	6.18×10^{-6}	0.883	3.40×10^3
Fe805	19.62	4.272×10^{-5}	0.747	8.964	1.335×10^{-4}	0.775	4.915×10^3

Figure 6 shows the corroded surface morphologies and topographic maps of the specimens at the different annealed temperatures after removing the products of the biodegradation, which were immersed in Hank's solution for 14 days. The corroded surfaces were relatively intact and compact, and the dimly discernible biodegradation became lighter with the increase of the annealed temperature, as shown in Figure 6a–c. The corroded topographic maps, as shown in Figure 6a₁–c₁, agreed with the corresponding corroded surface morphologies. There were some preferential small and shallow pits when annealed at 765 °C and 785 °C (Figure 6a₁,b₁), while there was relatively more uniform on a macro-scale when annealed at 805 °C (Figure 6c₁).

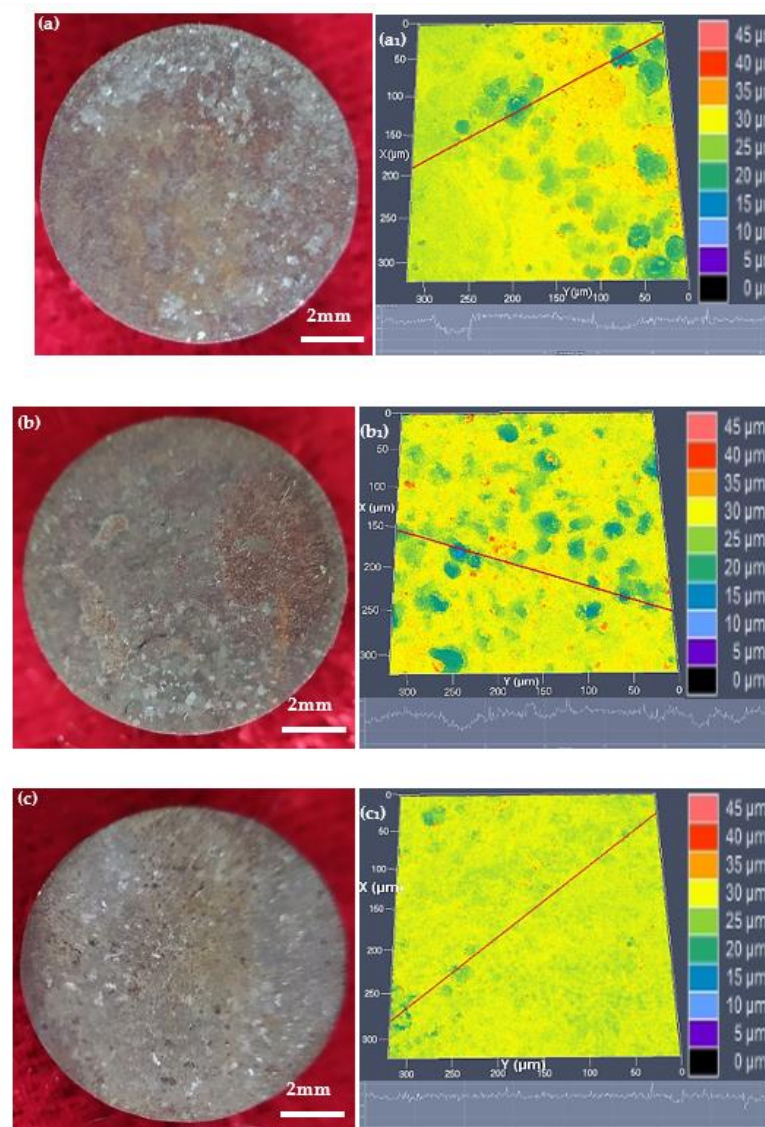


Figure 6. Surface morphologies ((a–c)) and topographic maps ((a₁–c₁)) of the different annealed conditions: (a,a₁) for annealed at 765 °C, (b,b₁) for annealed at 785 °C, (c,c₁) for annealed at 805 °C.

Table 3 shows the biodegradation rate, P_i , of the specimens at different annealed temperatures that were calculated by Equation (1) using the measured i_{corr} data, and the biodegradation rate, P_w , of the specimens at the different annealed temperatures that were calculated by Equation (2) and Equation (3) using the weight loss data. The corresponding initially forged data were also listed in Table 3 as the controls. The P_i value or the P_w value of the initial forged condition was relatively high. Those of the specimens at the different annealed temperature decreased with the increase of the annealed temperature.

Table 3. Biodegradation rate of the initial forged and different annealed conditions in Hank's solution.

Specimen No.	P_i (mm y ⁻¹)	P_w (mm y ⁻¹)
Initial forged condition	0.0718	0.207 ± 0.6
Fe765	0.0523	0.170 ± 0.5
Fe785	0.0392	0.147 ± 0.3
Fe805	0.0245	0.128 ± 0.3

4. Discussion

4.1. Grain Growth upon Annealing

Ferrite grain growth upon annealing is a cannibalistic process. The growth of some grains must be accommodated by the shrinkage and ultimate disappearance of other grains. The increase of the average ferrite grain size decreases the area of grain boundary and thus decreases the energy of grain boundary. For pure iron, the circumstance of the grain grown upon annealing is almost entirely decided by the decrease of grain boundary energy, because the influence of other structural factors, such as impure inclusions, macro-segregations and second phase particles, may be negligible. The EBSD characterized ferrite grain boundaries well described the new undistorted ferrite grains with little residual stress and low dislocation density upon annealing, i.e., the growth of ferrite grains. Therefore, the driving force of the ferrite grain growth is the reduction of the grain boundary energy [18], indicated as:

$$F_d = 2 \frac{\gamma}{R} \quad (5)$$

where F_d is the driving force of grain growth, γ is grain boundary energy and R is grain size.

From a thermo-dynamic viewpoint, the grain growth kinetic is assumed to obey an Arrhenius relation:

$$\frac{dR}{dt} = AF_d \exp(-Q/KT) \quad (6)$$

where A is constant, Q is the activation energy of grain growth, k is gas constant and T is the absolute temperature.

Substituting Equation (5) into Equation (6)

$$\frac{dR}{dt} = 2A\gamma \exp(-Q/kT)/R \quad (7)$$

Based on some calculus relation assumptions

$$R^2 = 4A\gamma(t - C) \exp(-Q/kT) \quad (8)$$

where C is calculus constant. Therefore, the ferrite grain size increases with the increasing annealed temperature, which is substantiated by the present results, as depicted in Figure 2.

4.2. Biodegradation

The biodegradation rate of the specimens at the different annealed temperatures in Hank's solution was different, as stated above. This difference in biodegradation rate was primarily due to the evolution of ferrite grain size caused by annealing. The evolution of the ferrite grain size produced the change of the ferrite grain boundary area. The micro-segregation of the ferrite grain boundary occurred in pure iron (99.9%). The

standard electrode potential of iron is -0.44 V, which is usually higher than the main metal impurities in pure iron, such as Cr (-0.74), Mn (-1.179), Ti (-1.630) and Al (-1.663). Therefore, the potential at grain boundary with more metal impurities is lower than that of the pure iron matrix, and iron acts as cathode and grain boundary as anode. Reducing grain size is equivalent to increasing grain boundary area [19]. At this time, the biodegradation resistance decreases with decreasing grain size, because the biodegradation resistance of the grain boundary is low and the increase of grain boundary area reduces the biodegradation resistance. Therefore, the ferrite grain boundary largely influences the biodegradation of pure iron. Furthermore, the ferrite grain size (d) increased with increasing the annealed temperature, while the biodegradation rate (P_i or P_w) decreased with increasing the annealed temperature. Figure 7 depicts the plots of P_i versus $d^{-1/2}$ and P_w versus $d^{-1/2}$, in which the initial forged condition is also used as a control. The obtained plots synchronized well to achieve a monotonic character. The relationship between the P_i and the d was expressed as Equation (9) with a correlation coefficient of 0.97 and that between the P_w and the d was expressed as Equation (10) with a correlation coefficient of 0.94. As a result, the biodegradation rate of pure iron was linearly ferrite grain size-dependent, following a so-called Hall–Petch relation [14].

$$P_i = -0.04 + 0.55d^{-\frac{1}{2}} \quad (9)$$

$$P_w = 0.02 + 0.91d^{-\frac{1}{2}} \quad (10)$$

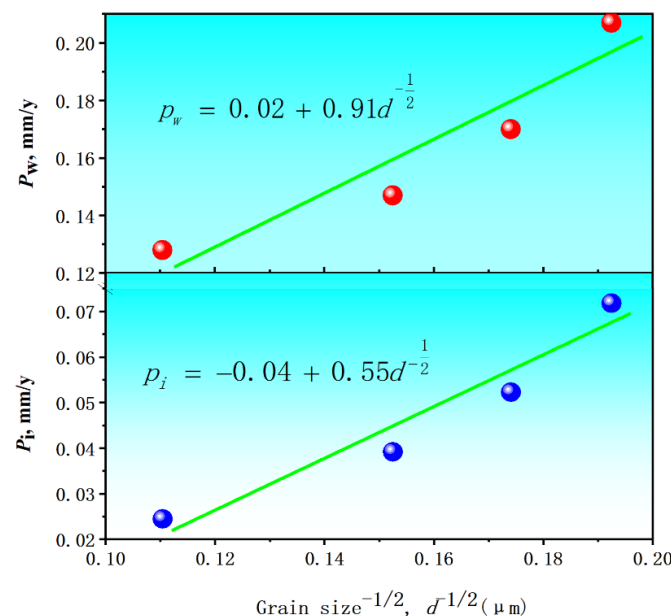


Figure 7. The relation between the biodegradation rate (P_i or P_w) and the average ferrite size (d).

4.3. Safe Intake and Toxicity

Acceptable safe intake and toxicity is essential for a biodegradable implant metal, which mainly relies on the biodegradation product toxicity [20], the released concentration of the metal ions [21], and the metal ions themselves against the cell metabolic activities [22]. As the biodegradation of pure iron occurs, the anodic reaction is expressed as: $\text{Fe} - 2e \rightarrow \text{Fe}^{2+}$ and the cathodic reaction is expressed as: $2\text{H}_2\text{O} + \text{O}_2 + 4e \rightarrow 4\text{OH}^{-1}$. Therefore, $\text{Fe}(\text{OH})_2$ is obtained according to $\text{Fe}^{2+} + 2\text{OH}^{-1} \rightarrow 2\text{Fe}(\text{OH})_2$ and subsequently the obtained $\text{Fe}(\text{OH})_2$ is easily oxidized to form $\text{Fe}(\text{OH})_3$ due to its instability according to $4\text{Fe}(\text{OH})_2 + 2\text{H}_2\text{O} + \text{O}_2 \rightarrow 4\text{Fe}(\text{OH})_3$. Furthermore, the Ca/P compounds usually precipitate on the hydroxide layer surface as the biodegradation proceeds [23]. All these biodegradation products are nontoxic [24]. The concentration of the released iron ions immersed in Hank's solution for 24 h was $2.52 \mu\text{g}/(\text{mL day})$ for the Fe765, which was the

maximum in the present annealed conditions due to its relatively high biodegradation rate. Iron as an element is essential for the human body. $\text{Fe}(\text{OH})_3$ or Fe^{3+} was produced during the biodegradation as described above. Fe^{3+} binds to the transferrin exclusively, and subsequently the iron-loaded transferrins are transported to the cell surface, where the iron ion is absorbed due to the endocytosis [25]. The average daily released iron ion concentration of Fe765 is maximum in the present annealed conditions and is $2.52 \mu\text{g}/(\text{mL day})$ as mentioned above, much lower than the value of the iron half-maximal inhibitory concentration (IC50) [21]. As reported, an iron ion concentration of less than $10 \mu\text{g}/(\text{mL day})$ had a favorable influence on the endothelial cell metabolic activity and less than $50 \mu\text{g}/(\text{mL day})$ had little inhibitory influence on the endothelial cell metabolic activities [26]. Therefore, the biocompatibility of the pure iron experiencing annealing is acceptable.

5. Conclusions

1. As annealed, the nuclei were generated at the sub-grain or grain boundaries of the original deformed microstructure, and the new undistorted ferrite grains with little residual stress and low dislocation density were formed.
2. A spectrum of ferrite grain size was gained by changing the annealed temperature. Hardness (HV) and biodegradation rate (P_i or P_w) were linearly ferrite grain size-dependent:
3. $\text{HV} = 58.9 + 383.2d^{-\frac{1}{2}}$; and $P_i = -0.04 + 0.55d^{-\frac{1}{2}}$ or $P_w = 0.02 + 0.91d^{-\frac{1}{2}}$.
4. The biocompatibility of the pure iron experiencing annealing is acceptable.
5. The obtained results were quite helpful for better regulating the biodegradation of biodegradable pure iron through annealing.

Author Contributions: Conceptualization, Y.Z.; Data curation, K.Z. and Z.Z.; Formal analysis, Z.Z.; Funding acquisition, W.L.; Investigation, Y.Z.; Project administration, W.L. and M.Z.; Resources, K.Z.; Writing—original draft, Y.Z. and Z.Z.; Writing—review & editing, M.Z. All authors have read and agreed to the published version of the manuscript.

Funding: This research was financially supported by Natural Science Foundation of China (No. 51874368).

Data Availability Statement: Not applicable.

Conflicts of Interest: Authors declare no conflict of interest.

References

1. Peuster, M.; Wohlsein, P.; Brugmann, M.; Ehlerding, M.; Seidler, K.; Fink, C.; Brauer, H.; Fischer, A.; Hausdorf, G. A novel approach to temporary stenting: Degradable cardiovascular stents produced from corrodible metal—Results 6–18 months after implantation into New Zealand white rabbits. *Heart* **2001**, *86*, 563–569. [[CrossRef](#)]
2. Salama, M.; Vaz, M.F.; Colaço, R.; Santos, C.; Carmezim, M. Biodegradable Iron and Porous Iron: Mechanical Properties, Degradation Behaviour, Manufacturing Routes and Biomedical Applications. *J. Funct. Biomater.* **2022**, *13*, 72. [[CrossRef](#)] [[PubMed](#)]
3. Peuster, M.; Hesse, C.; Schloo, T.; Fink, C.; Beerbaum, P.; von Schnakenburg, C.; von Schnakenburg, C. Long-term biocompatibility of a corrodible peripheral iron stent in the porcine descending aorta. *Biomaterials* **2006**, *27*, 4955–4962. [[CrossRef](#)]
4. Zhao, Y.; Feng, J.; Yu, H.; Lin, W.; Li, X.; Tian, Y.; Zhao, M. Comparative Study on Biodegradation of Pure Iron Prepared by Microwave Sintering and Laser Melting. *Materials* **2022**, *15*, 1604. [[CrossRef](#)]
5. Carluccio, D.; Bermingham, M.; Kent, D.; Demir, A.G.; Previtali, B.; Dargusch, M.S. Comparative study of pure iron manufactured by selective laser melting, laser metal deposition, and casting processes. *Adv. Eng. Mater.* **2019**, *21*, 1900049.
6. Bagherifard, S.; Beni, R.N.; Kajaneck, D.; Donnini, R.; Monti, S.; Molla, M.F.; Hadzima, B.; Guagliano, M. Inclined and multi-directional surface impacts accelerate biodegradation and improve mechanical properties of pure iron. *J. Mech. Behav. Biomed. Mater.* **2021**, *119*, 104476. [[CrossRef](#)]
7. Obayi, C.S.; Tolouei, R.; Paternoster, C.; Turgeon, S.; Okorie, B.A.; Obikwelu, D.O.; Cassar, G.; Buhagiar, J.; Mantovani, D. Influence of cross-rolling on the micro-texture and biodegradation of pure iron as biodegradable material for medical implants. *Acta Biomater.* **2015**, *17*, 68–77. [[CrossRef](#)]
8. Batista, B.A.; Soares, R.B.; Lins, V.D.C.; Figueiredo, R.B.; Hohenwarter, A.; Matencio, T. Corrosion in hank's solution and mechanical strength of ultrafine-grained pure iron. *Adv. Eng. Mater.* **2020**, *22*, 2000183. [[CrossRef](#)]

9. Obayi, C.S.; Tolouei, R.; Mostavan, A.; Paternoster, C.; Turgeon, S.; Okorie, B.A.; Obikwelu, D.O.; Mantovani, D. Effect of grain sizes on mechanical properties and biodegradation behavior of pure iron for cardiovascular stent application. *Biomater* **2014**, *6*, e959874. [[CrossRef](#)]
10. Zhao, Y.; Tang, Y.; Zhao, M.; Liu, L.; Gao, C.; Shuai, C.; Zeng, R.; Atrens, A.; Lin, Y. Graphene Oxide Reinforced Iron Matrix Composite with Enhanced Biodegradation Rate Prepared by Selective Laser Melting. *Adv. Eng. Mater.* **2019**, *21*, 1900314. [[CrossRef](#)]
11. Deng, B.; Guo, Y.; Zhao, M.-C.; Li, Q.-F.; Ma, B.; Duan, B.; Yin, D.; Atrens, A. Study on a Novel Biodegradable and Antibacterial Fe-Based Alloy Prepared by Microwave Sintering. *Materials* **2021**, *14*, 3784. [[CrossRef](#)]
12. Tian, Y.; Zhao, M.; Liu, W.; Zhang, J.; Zhang, M.; Li, H.; Yin, D.; Atrens, A. Comparison on Tensile Characteristics of Plain C–Mn Steel with Ultrafine Grained Ferrite/Cementite Microstructure and Coarse Grained Ferrite/Pearlite Microstructure. *Materials* **2021**, *14*, 2309. [[CrossRef](#)]
13. Xie, B.; Zhao, M.-C.; Tao, J.-X.; Zhao, Y.-C.; Yin, D.; Gao, C.; Shuai, C.; Atrens, A. Comparison of the biodegradation of ZK30 subjected to solid solution treating and selective laser melting. *J. Mater. Res. Technol.* **2020**, *10*, 722–729. [[CrossRef](#)]
14. Hansen, N. Hall–Petch relation and boundary strengthening. *Scr. Mater.* **2004**, *51*, 801–806. [[CrossRef](#)]
15. Zhang, W.; Zhao, M.; Wang, Z.; Tan, L.; Qi, Y.; Yin, D.; Yang, K.; Atrens, A. Enhanced initial biodegradation resistance of the biomedical Mg–Cu alloy by surface nanomodification. *J. Magnes. Alloy.* **2022**, *in press*. [[CrossRef](#)]
16. Zheng, Z.; Zhao, M.-C.; Tan, L.; Zhao, Y.-C.; Xie, B.; Huang, L.; Yin, D.; Yang, K.; Atrens, A. Biodegradation behaviour of hydroxyapatite-containing self-sealing micro-arc-oxidation coating on pure Mg. *Surf. Eng.* **2021**, *37*, 942–952. [[CrossRef](#)]
17. Wang, K.; Yin, D.; Zhao, Y.-C.; Atrens, A.; Zhao, M.-C. Microstructural evolution upon heat treatments and its effect on corrosion in Al–Zn–Mg alloys containing Sc and Zr. *J. Mater. Res. Technol.* **2020**, *9*, 5077–5089. [[CrossRef](#)]
18. Sinha, A.K. *Physical Metallurgy Handbook*; McGraw-Hill Press: New York, NY, USA, 2003; Chapter 5; p. 40.
19. Qu, Z.; Liu, L.; Deng, Y.; Tao, R.; Liu, W.; Zheng, Z.; Zhao, M.-C. Relationship between Biodegradation Rate and Grain Size Itself Excluding Other Structural Factors Caused by Alloying Additions and Deformation Processing for Pure Mg. *Materials* **2022**, *15*, 5295. [[CrossRef](#)] [[PubMed](#)]
20. Gu, X.; Zheng, Y.; Cheng, Y.; Zhong, S.; Xi, T. In vitro corrosion and biocompatibility of binary magnesium alloys. *Biomaterials* **2009**, *30*, 484–498. [[CrossRef](#)] [[PubMed](#)]
21. Yamamoto, A.; Honma, R.; Sumita, M. Cytotoxicity evaluation of 43 metal salts using murine fibroblasts and osteoblastic cells. *J. Biomed. Mater. Res.* **1998**, *39*, 331–340. [[CrossRef](#)]
22. Hermawan, H.; Purnama, A.; Dube, D.; Couet, J.; Mantovani, D. Fe–Mn alloys for metallic biodegradable stents: Degradation and cell viability studies. *Acta Biomater.* **2010**, *6*, 1852–1860. [[CrossRef](#)] [[PubMed](#)]
23. Zhao, Y.; Tang, Y.; Zhao, M.; Liu, C.; Liu, L.; Gao, C.; Shuai, C.; Atrens, A. Study on Fe-xGO composites prepared by selective laser melting: Microstructure, hardness, biodegradation and Cytocompatibility. *JOM* **2020**, *72*, 1163–1174. [[CrossRef](#)]
24. Yusop, A.H.; Daud, N.M.; Nur, H.; Kadir, M.R.A.; Hermawan, H. Controlling the degradation kinetics of porous iron by poly(lactic-co-glycolic acid) infiltration for use as temporary medical implants. *Sci. Rep.* **2015**, *5*, 11194. [[CrossRef](#)]
25. Guo, Y.X.; Zhao, M.C.; Xie, B.; Zhao, Y.C.; Yin, D.F.; Gao, C.D.; Shuai, C.J.; Atrens, A. In vitro Corrosion resistance and antibacterial performance of novel Fe-xCu biomedical alloys prepared by selective laser melting. *Adv. Eng. Mater.* **2021**, *23*, 2001000. [[CrossRef](#)]
26. Zhu, S.; Huang, N.; Xu, L.; Zhang, Y.; Liu, H.; Sun, H.; Leng, Y. Biocompatibility of pure iron: In vitro assessment of degradation kinetics and cytotoxicity on endothelial cells. *Mater. Sci. Eng. C* **2009**, *29*, 1589–1592. [[CrossRef](#)]